Journal of Biomedical Optics

BiomedicalOptics.SPIEDigitalLibrary.org

Tri-band spectroscopic optical coherence tomography based on optical parametric amplification for lipid and vessel visualization

Luoqin Yu
Jiqiang Kang
Chandra Jinata
Xie Wang
Xiaoming Wei
Kin Tak Chan
Nikki P. Lee
Kenneth K. Y. Wong

SPIE.

Tri-band spectroscopic optical coherence tomography based on optical parametric amplification for lipid and vessel visualization

Luoqin Yu,[a] Jiqiang Kang,[a] Chandra Jinata,[a] Xie Wang,[a] Xiaoming Wei,[a] Kin Tak Chan,[b] Nikki P. Lee,[b] and Kenneth K. Y. Wong[a,*]
[a]The University of Hong Kong, Photonic Systems Research Laboratory, Department of Electrical and Electronic Engineering, Pokfulam Road, Hong Kong, China
[b]The University of Hong Kong, Department of Surgery, Hong Kong, Pokfulam Road, Hong Kong, China

Abstract. A tri-band spectroscopic optical coherence tomography (SOCT) system has been implemented for visualization of lipid and blood vessel distribution. The tri-band swept source, which covers output spectrum in 1.3, 1.5, and 1.6 μm wavelength windows, is based on a dual-band Fourier domain mode-locked laser and a fiber optical parametric amplifier. This tri-band SOCT can further differentiate materials, e.g., lipid and artery, qualitatively by contrasting attenuation coefficients difference within any two of these bands. Furthermore, *ex vivo* imaging of both porcine artery with artificial lipid plaque phantom and mice with coronary artery disease were demonstrated to showcase the capability of our SOCT. [DOI: 10.1117/1.JBO.20.12.126006]

Keywords: optical coherence tomography; optical parametric amplification; spectroscopic imaging; tri-band source.

Paper 150538R received Aug. 10, 2015; accepted for publication Nov. 12, 2015; published online Dec. 16, 2015.

1 Introduction

Optical coherence tomography (OCT) is a promising imaging modality with many benefits, e.g., high resolution, fast scan rate, label-free operation, and noninvasive biopsy, so that video-rate *in vivo* three-dimensional imaging becomes possible. It has strategically filled the gap between confocal microscopy and ultrasound imaging with moderate imaging depth and micrometer-scale resolution. In fact, numerous studies since 1991 have applied this technology to different clinical applications.[1] In addition to its promise, conventional OCT technology primarily only provides intensity contrast data for clinicians to diagnose, which results in indirect outcome and further needs professional experience. It also suffers from limited information regarding plaque compositions.[2] Nowadays, functional OCT extends its capability by providing more direct diagnostic information. Some of the examples are Doppler OCT (DOCT), which focuses on measuring the blood flow rate by utilizing Doppler principle; polarization-sensitive OCT (PS-OCT), which offers tissue birefringence information by utilizing polarization-sensitive detection; and spectroscopic OCT (SOCT), a high-potential functional OCT, which obtains morphologic and spectroscopic information simultaneously by distinguishing scattering and absorption properties from different materials.[3]

Due to its unique feature, researchers have investigated SOCT application in various fields from determination of localized tissue oxygenation[4] to material differentiation, such as types of liquids[5] or biological tissue.[6–9] One of the highlights in these applications lies in assisting the diagnosis process of coronary artery disease (CAD), one of the common fatal diseases in developed countries. OCT is a promising tool to identify vulnerable plaques, especially for the thin-cap fibroatheroma that has thickness <65 μm.[2] Additionally, the ability to differentiate types of plaques is also preferable for further therapeutic interventions. As a result, SOCT is proposed to be one of the major pathology diagnostic tools. Previously, Tanaka et al.[8] have developed a spectral domain OCT (SD-OCT) to image lipid distribution within blood vessel by applying a broadband source centered at 1.7 μm that covered both low- and high-lipid absorption and providing signal differences among the subband images. However, this system required two spectrometers and subband division that it was not only costly but also computationally inefficient. In addition, it suffered from transmission loss as commercial products for this wavelength band are not favorable. Another single-band SOCT used to identify artery plaques has also been reported by Fleming et al. They demonstrated an optical frequency domain imaging system by applying a 1.3 μm swept source and quadratic discriminant analysis model, which was likewise computationally demanding.[9]

Instead of using single-band SOCT illumination that requires stringent wavelength band selection and large bandwidth, multiband SOCT provides more flexibility. The dual-band SOCT was originally proposed by Schmitt et al.[5] by ratiometric processing of the measured interference signals to distinguish lipid and water. It required a pair of light-emitting diodes emitting in and outside the vibrational absorption band of the chemical compound separately. Regarding the spectroscopic contrast, tri-band system with additional information from the third wavelength band can further enhance the contrast. For example, some researchers construct images from three bands in red (R), green (G), and blue (B) channels to obtain three-color images.[10] Other multiband OCT systems have been demonstrated with filtered single broadband source,[10] filtered supercontinuum laser

*Address all correspondence to: Kenneth K. Y. Wong, E-mail: kywong@eee.hku.hk

1083-3668/2015/$25.00 © 2015 SPIE

sources,[11] common-path broadband source,[12] and different broadband sources.[5] Our group has previously reported a dual-band OCT system based on parametric amplified Fourier domain mode-locked (FDML) laser with time-multiplexing scheme[13] and a dual-band FDML laser OCT system with wavelength-division multiplexing (WDM).[14] FDML lasers have significant advantages in OCT applications since fast wavelength sweeping, wide tuning range, narrow instantaneous linewidth, and proper output power can be obtained at the same time.[15] Fiber optical parametric amplifier (OPA) can be incorporated in multiband SOCT systems as it not only contains a broad amplification window but also offers additional output range at idler band that is phase-matched with the signal band.[16] The sweeping ranges can thus outperform traditional wavelength bands that are limited by intracavity amplifiers in FDML lasers.

To improve the functionality of our system, we incorporated the dual-band FDML laser together with fiber OPA to attain a new sweeping range. The swept source renders a simultaneous tri-band swept source output with center wavelengths at 1.3, 1.5, and 1.6 μm. *Ex vivo* experiments on both porcine and mouse models were also demonstrated to visualize lipid and blood vessel distribution.

2 Principle

2.1 *Tri-band Spectroscopic Optical Coherence Tomography to Distinguish Lipid and Artery*

Various methods have been introduced for SOCT-based tissue characterization.[5,17] This is due to the fact that different materials have distinguishable absorption and scattering coefficients at different wavelengths. Time frequency analysis, including short-time Fourier transform, wavelet transform, the Wigner–Ville distribution, and the dual-window methods, is usually applied to a single-band SOCT, but a spectral/spatial tradeoff is still inevitable.[18] In the meantime, a proper wavelength range is required to provide contrast between subbands.[8] Other than that, wavelength selection in multiband SOCT is more attainable to offer facile image contrast. Schmitt et al.[5] concluded that the attenuation coefficients of a sample at two separate wavelength bands can be expressed as

$$\alpha_i(z) - \alpha_j(z) = \frac{1}{2}\frac{\mathrm{d}}{\mathrm{d}z}\ln\left[\frac{I_j(z)}{I_i(z)}\right] = \frac{1}{2(z-z_0)}\ln\left[\frac{I_j(z)}{I_i(z)}\right], \tag{1}$$

where α_i is the attenuation coefficient at band i, z is the corresponding depth defined by light path length difference between sample and reference arms, z_0 is the reference depth where signal intensities are normalized, and $I_i(z)$ is the light intensity at depth z. By setting $\Delta\alpha(z) = \alpha_i(z) - \alpha_j(z)$,

$$\frac{I_i(z)}{I_j(z)} = \mathrm{e}^{-i2\Delta\alpha(z-z_0)}. \tag{2}$$

Therefore, by dividing the normalized intensity of sample images obtained from different wavelengths pixel-by-pixel, negative-correlated attenuation coefficient difference between the two bands could be obtained with relative depth. In this work, we justified the qualitative capability of this tri-band SOCT so that it can differentiate lipid and artery by contrasting attenuation coefficient difference between 1.3/1.5 and 1.5/1.6 μm.

Tanaka et al. first investigated basic constituents present in a CAD-related artery model.[8] The components have specific attenuation reflection spectra (Fig. 1). The lipid category itself consists of lard and cholesterol. Furthermore, as the tri-band swept source allows extra contrast from the attenuation coefficient differences with the third band, this particular advantage was consequently utilized to visualize artery vessel and lipid plaques independently.

From Fig. 1, attenuation coefficients at different wavelengths of these constituents can be intuitively compared. Figure 2 lists both approximate average attenuation coefficients in target wavelength ranges shown in Fig. 1 and attenuation coefficients difference between any two of these bands. As intensity ratio has a negative correlation with this difference, the intensity ratios are listed out by negative attenuation coefficient difference of corresponding wavelengths, namely $-\Delta\alpha$. The contrast principle applies to all $\Delta\alpha$, including negative attenuation coefficient differences. Larger ratios are highlighted by colors where those could be extracted more accurately in ratiometric images.

Both 1.3/1.5 and 1.3/1.6 μm are able to exhibit artery distribution, while the 1.3/1.5 μm ratiometric image would render a higher contrast by comparing $-\Delta\alpha$ values of artery and lipid constituents ($-\Delta\alpha = 8$ to 0 versus $-\Delta\alpha = 4$ to -1). Therefore the artery distribution, which was highlighted in red, could be visualized by selecting areas with higher contrast in 1.3/1.5 μm ratiometric image. In a similar way, by selecting higher ratio areas in ratiometric images of 1.5/1.6 μm, lipid distribution was foreseen in blue. By combining the images together, a complete lipid and artery distribution image were obtained from

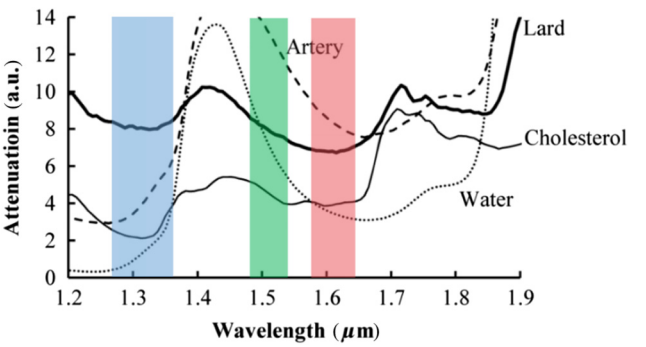

Fig. 1 Infrared spectra of lipids (lard and cholesterol), normal artery, and water with distinctive wavelength bands. Blue: 1.3 μm band; green: 1.5 μm band; and red: 1.6 μm band. Reproduced with permission © 2015 Optical Society of America.[8]

	Material α (a.u.)			Material $-\Delta\alpha$ (a.u.)		
Wavelength (μm)	1.3	1.5	1.6	$\frac{I_{1.3}(z)}{I_{1.5}(z)}$	$\frac{I_{1.3}(z)}{I_{1.6}(z)}$	$\frac{I_{1.5}(z)}{I_{1.6}(z)}$
Artery	5	13	9	8	4	-4
Lard	8	8	7	0	-1	-1
Cholesterol	3	4	4	1	1	0
Water	2	8	4	6	2	-4

Fig. 2 Comparison of material attenuation coefficients at different wavelength bands. The second to fourth column: attenuation coefficient or α; the fifth to seventh column: attenuation coefficient difference or $-\Delta\alpha$. Larger $-\Delta\alpha$ are highlighted with colors. Artery is represented by red and blue represents lipid.

the tri-band SOCT setup. The detailed image processing procedures are described in Sec. 3.4.

3 Setup and Processing

3.1 *Setup of the Tri-band Swept Source*

The tri-band swept source was composed of a dual-band FDML laser with output wavelength bands at 1.3 and 1.6 μm and incorporated with the OPA to provide an additional idler band at 1.5 μm (Fig. 3). The gain medium in the FDML was a semiconductor optical amplifier (SOA, Inphenix) centered at 1310 nm. In the meantime, a booster optical amplifier (BOA, Covega) centered at 1625 nm was used as gain medium in the 1.6 μm band. Two isolators next to the gain medium were inserted to ensure one-directional light propagation in the cavity. A polarization controller was used to control polarization state in both the bands. This was carried out to ensure that the polarization state matches with the gain medium. Two fiber Fabry–Perot tunable filters (FFP-TF, Micron Optics) at O and C bands were utilized for active wavelength selection. The bands were controlled by a customized dual-band driver to sweep at the same frequency simultaneously; nevertheless, the driver can set different bias and peak-to-peak values at either band. A spool of 4.5-km single-mode fiber (SMF28e, Corning), which has a resonating frequency at ~45 kHz, was used as common delay fiber in both cavities. It should be noted that the round-trip time of light in two cavities were set identical by matching the lengths of two cavities. Two broadband 1310/1550 WDM couplers were employed to separate light at different wavelength bands. The output of the 1.3 μm was amplified by another booster amplifier (BOA, COVEGA) and optical parametric amplification was incorporated for the 1.6 μm band.

The 1.6 μm FDML laser output acted as the signal band in the OPA configuration. By both selecting the optimized pump wavelength at 1555.3 nm and aligning the polarization in line with the phase modulator (PM), a continuous-wave (CW) signal from a tunable laser source was then modulated by the PM with $2^{15} - 1$ pseudo-random binary sequence signal. After two-stage erbium-doped fiber amplifiers (EDFAs) and a tunable bandpass filter applied to suppress noise level, the high-power CW pump was then coupled to a WDM coupler together with the FDML laser signal in L band. A high-power circulator was inserted to monitor stimulated Raman scattering level with a power meter and ensure optimized tuning. A 150-m highly nonlinear dispersion-shift fiber (HNL-DSF) with zero-dispersion wavelength at 1554.7 nm and nonlinear coefficient of 14 $W^{-1}\,km^{-1}$ played a role as nonlinear gain medium in OPA. Signal from FDML laser was subsequently amplified by OPA. An additional idler, which had phase-matched interaction with the FDML laser signal, was generated in the meantime while passing through the HNL-DSF. A WDM coupler and fiber-Bragg grating were adapted to filter out the redundant CW pump. Finally, the 1.6 μm signal and 1.5 μm idler were separated by a C/L band WDM coupler and eventually utilized for OCT imaging.

3.2 *Setup of the Imaging System*

Figure 4 depicts schematic diagram of the imaging system. Ten percent of the output in each band was split off and coupled to two Mach–Zehnder interferometers (MZIs) with center wavelengths at 1310 and 1550 nm (INT-MZI-1310, INT-MZI-1550, respectively, Thorlabs) for time-frequency calibration. It should be noted that time multiplexing by adding proper lengths of fiber at any two bands could be implemented to alleviate cost and complexity. Hereby, the sample was successively illuminated by the three wavelength bands. This technique was successfully demonstrated in our previous work on dual-band OCT.[13] As a proof-of-concept study, we manually launched each band into a 10/90 coupler (CP5) to achieve similar results. The source was then divided by the 90/10 coupler with 90% power launched into sample arm and 10% power launched into reference arm. After collecting signals from both arms and passing those signals through two optical circulators and a WDM coupler, interference signal was detected by a balance detector, which could cancel out excess photon noise. The black solid lines in Fig. 4 indicate optical fiber, while the blue lines refer to electrical cables that transmit electronic signal.

In the detection part, a digitizer (ATS460, Alazar Tech) with 125 MS/s sampling rate was used to convert analog-to-digital signal. The system setting and data capturing were controlled by a LabVIEW programing interface (National Instrument), while image analysis was processed in MATLAB (MathWorks, Natick, Massachusetts). Further description about the detection setup was delivered by Xu et al.[14]

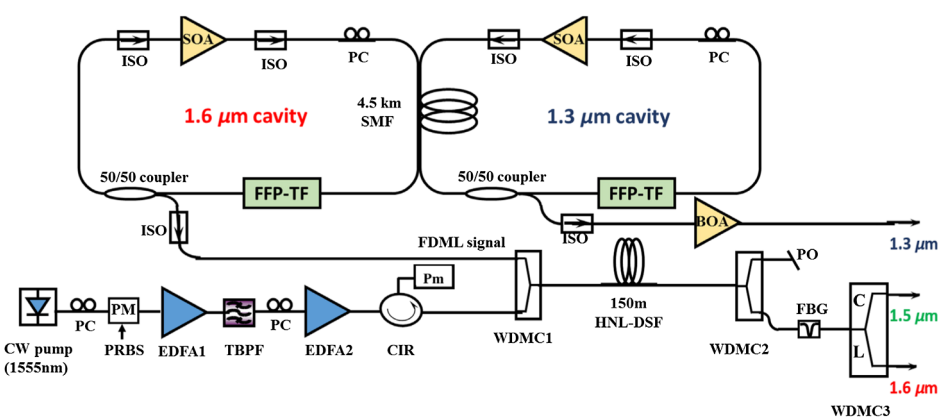

Fig. 3 Setup of the tri-band swept source. FFP-TF, fiber Fabry–Perot tunable filter; ISO, isolator; SMF, single-mode fiber; SOA, semiconductor optical amplifier; BOA, booster optical amplifier; EDFA, erbium-doped fiber amplifier; WDMC, wavelength-division multiplexer coupler; TBPF, tunable bandpass filter; PC, polarization controller; TLS, tunable laser source; HNL-DSF, highly nonlinear dispersion-shift fiber; FBG, fiber-Bragg grating filter; PM, phase modulator; and Pm, power meter.

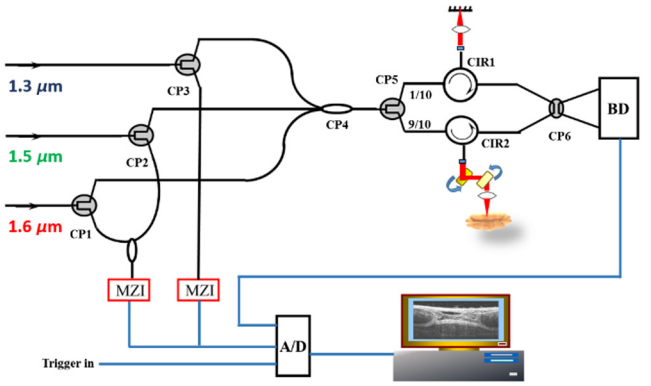

Fig. 4 Schematic diagram of the tri-band SOCT imaging system. CIR, circulator; CP, coupler; MZI, Mach–Zehnder interferometer; BD, balanced detector; and A/D, digitizer.

3.3 *Sample Preparation*

First for a porcine model, an artery phantom was created by obtaining a piece of porcine artery vessel from a local market and subsequently immersing it in saline solution for 22 h. The artery was then cut open in order to expose its inner side to the scanning light beam. Mayonnaise (Kraft), previously utilized by Fleming et al.,[9] and butter (Anchor) were selected as representative materials of the artificial lipid plaques. Both were injected into a nylon tube with both side blocked by thermal gels and placed next to the artery phantom [Fig. 5(b)], or those were spread on top of the artery directly [Fig. 5(d)].

Subsequently for mouse model, 8-week-old female C57BL/6 mice with apolipoprotein E-deficiency (apoE−/−) ($n = 3$) from The Jackson Laboratory (Bar Harbor, Maine) were used to demonstrate the capability of SOCT in differentiating blood vessel and lipid *ex vivo*. This particular knock-out mouse shows defect

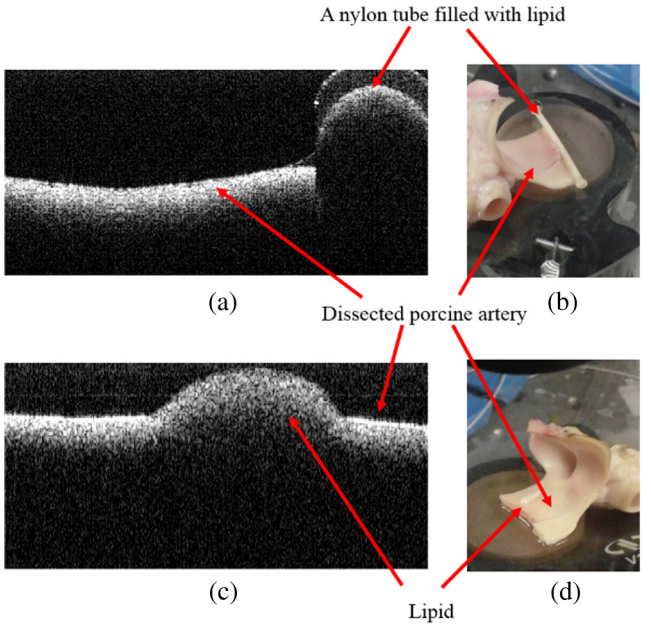

Fig. 5 Conventional OCT image and photographs of the porcine artery phantom and the lipid phantom used for tri-band imaging. (a) and (b) lipid was injected in a nylon tube and placed next to the dissected artery; (c) and (d) lipid was spread directly onto the dissected artery.

in clearing of plasma lipoproteins so that it can develop atherosclerosis rapidly.[19] Additionally, an 8-week-old female wild-type C57BL/6 mouse was also used as a negative control. All the animal experiments were approved by the committee on the use of live animals for teaching and research of The University of Hong Kong. After being sacrificed, aorta from each mouse was isolated and separated from perivascular adipose tissues. These samples were then immersed in formaldehyde (4%) for 2 days and phosphate-buffered saline (PBS) for preservation purpose. For histology examination, lipid staining—Oil Red O staining—was carried out. The aorta was first washed by 60% isopropanol for 1 min, stained by 0.3% Oil Red O (Sigma 09755) for 20 min, and finally washed by 60% isopropanol for 5 min before histology imaging.

3.4 *Measurement Procedure and Signal-Processing*

Figure 6 presents SOCT procedures to acquire spectral differentiated images of the samples. They are described as: (1) Data capturing: 1024 samples were captured by digitizer in each A-line with an A-scan rate of ~45 kHz of the tri-band swept source. For each frame, 1000 A-lines were used to construct an OCT image, resulting in a frame rate of ~45 Hz in real-time. (2) Resampling interference signals: OCT interference signals were resampled equally in wavenumber domain by extracting the phase information from the MZI calibration signal with Hilbert transform. (3) Windowing: interference signals from each A-line was smoothed by applying a Hanning Window. (4) Fourier transform: each A-line was then zero-padded to 2048 points and went through fast Fourier transform. Images were displayed by selecting the region of interest and presented in logarithmic scale. (5) Normalization: signal intensities at an assuming depth z_0 were set to unity by normalizing the top 1% highest pixel values that appear near air–tissue interface in each image. Pixel values of background were averaged and set to zero. (6) Ratiometric processing: $I_i(z)/I_j(z)$ was calculated pixel-by-pixel by offsetting 0.1 to all the normalized pixel values in order to get rid of zero denominator. (7) Filtering: a Gaussian low-pass filter was then applied to $I_{1.3}/I_{1.5}$ and $I_{1.5}/I_{1.6}$ ratiometric images by selecting proper filter parameters. These ratios were then contrast stretched and filtered by

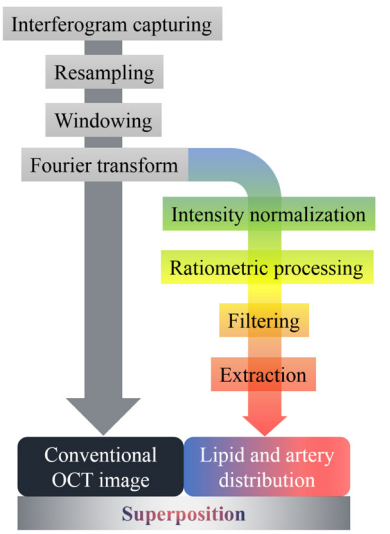

Fig. 6 Flow chart of the processing procedures for tri-band SOCT imaging.

a decision threshold. Ratio values above this threshold were kept. (8) Staining: ratiometric images were stained by pixel-by-pixel subtraction between the filtered $I_{1.3}/I_{1.5}$ and $I_{1.5}/I_{1.6}$. The subtraction would make target regions have large absolute values either positive or negative, while background regions have small absolute values. Blue color and red color were then coded at the color bar for visualization of both minimum and maximum values, which is lipid and artery region, correspondingly. It should be noted that if materials do not have contrast attenuation coefficient difference, color bar for the image needs to be rescaled for background normalization. (9) Superposition: distribution of different constituents was visualized on top of the original black/white OCT images by superposing the conventional OCT image and the colored SOCT image.

Specific for the mouse model, the sample arm at SOCT was replaced by a custom-made probe interface unit containing a fiber-optic rotary joint and a fiber-optic imaging catheter (Dragonfly, St. Jude Medical). Synchronized circumferential scanning was performed with all wavelength bands in order to get the cross-sectional images of the aorta. It should be noted that the imaging procedure was carried out within PBS for sample preservation purpose. After the SOCT imaging, each aorta was stained by Oil Red O and subsequently the sample was longitudinally opened and histology image was observed (Leica MZ75).

4 Results and Discussion

4.1 *Output of the Tri-band Swept Source*

The output spectrum measured by an optical spectrum analyzer (OSA) in the peak-hold mode is shown in Fig. 7. The output power was attenuated at each band to ensure OSA safety. It can be observed that the 1.3 μm band spanned from 1265 to 1365 nm, while the idler and signal band spanned from 1478 to 1540 nm and 1570 to 1640 nm, respectively. The measured resolutions were ~12, ~34, and ~48 μm for the 1.3, 1.5, and 1.6 μm bands, respectively. Because of unfiltered residual pump and limited separation ratio of the WDMC3 (Fig. 3), there was some power leakage of the idler to the signal band, which is identified as few spikes around 1550 nm (Fig. 7). The leakage is considered as background noise in the idler band imaging.

By setting BOA pump current at 250 mA and power at ~2.5 W, the output power measured after the amplification was ~35 mW for each band. Considering the split power and coupling loss, the power on the sample was ~10 mW, where thermal noise is not severe. Sensitivity values for 1.3, 1.5, and 1.6 μm bands were 94, 84, and 85 dB, respectively, while a short-noise limited theoretical value is calculated as 108 dB.[20] Reducing coupling and fiber component loss and further averaging the frame will help to increase the system sensitivity. The decreased sensitivity of signal and idler bands comparing to 1.3-μm band can be partially explained by amplified spontaneous emission noise from two EDFAs, extra loss from WDMCs, and their limited suppression ratio. In addition, intensity differences among different bands were corrected by normalization in postprocessing, when tissue attenuation difference is mainly relied on and can be ensured by optimal system setting.

4.2 *Spectroscopic Optical Coherence Tomography Imaging Results*

Figure 8 shows SOCT results of the porcine model processed by algorithms described in Sec. 3.4. Figures 8(a), 8(c), 8(e), and 8(g) are the typical OCT images obtained from 1.3 μm band, while Figs. 8(b), 8(d), 8(f), and 8(h) are color-encoded SOCT images processed with the above-mentioned procedures corresponding to Figs. 8(a), 8(c), 8(e), and 8(g), respectively. Among them, the top four images (a–d) have artificial lipid plaque made by butter, and the bottom four (e–h) images have artificial plaques made by mayonnaise. The butter has 81.4% fat contents, which is mainly composed by saturated fat. Meanwhile, mayonnaise has 76.2% fat contents and it is mainly composed by soybean oil that has a similar lipid composition to coronary lipid plaques.[9] It can be observed that different components are clearly distinguished by the proposed tri-band system. The artery region identified by SOCT is colored by red hue, while blue hue represents lipid region.

Furthermore, mouse model was also imaged by the tri-band OCT endoscopy. Figure 9(c) shows that healthy aorta exhibited a blue background in the prestaining, which has a distinctive feature comparing to the CAD aorta image where artery was stained in red and lipid was presented in blue. This is because the healthy model only contains water (PBS) and artery, both of which have $-\Delta\alpha = -4$ without much contrast derived from $I_{1.5}/I_{1.6}$. Thus, there was no proper threshold for region selection and highest ratios are spreading in the image. After Gaussian filtering, normalization, and subtraction by $I_{1.3}/I_{1.5}$, negative value pixels exhibited blue-biased background. After

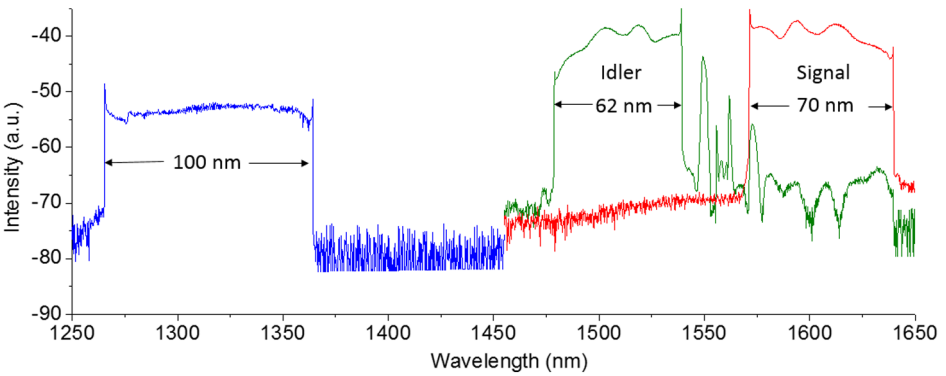

Fig. 7 Measured output spectrum of the three separate bands. Blue: 1.3 μm band; green: 1.5 μm band; and red: 1.6 μm band.

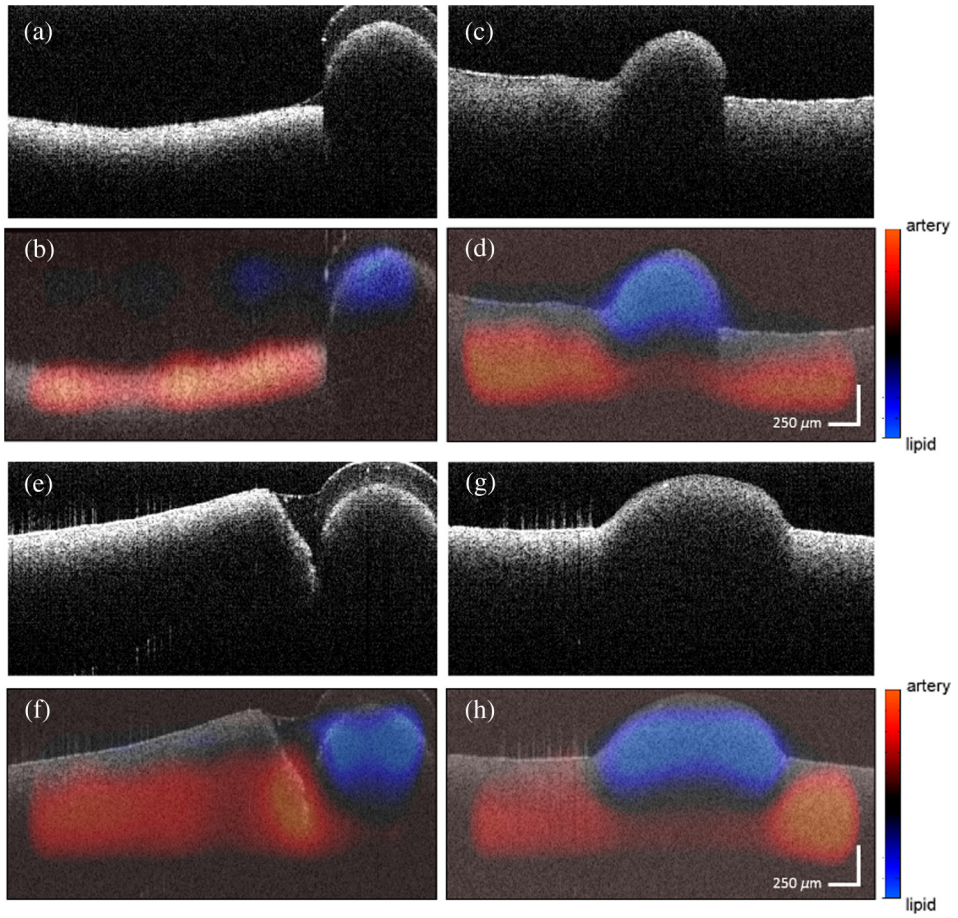

Fig. 8 SOCT imaging results. (a), (c), (e), (g) conventional OCT images from 1.3 μm band. (b), (d), (f), (h) SOCT images corresponding to (a), (c), (e), (g), respectively.

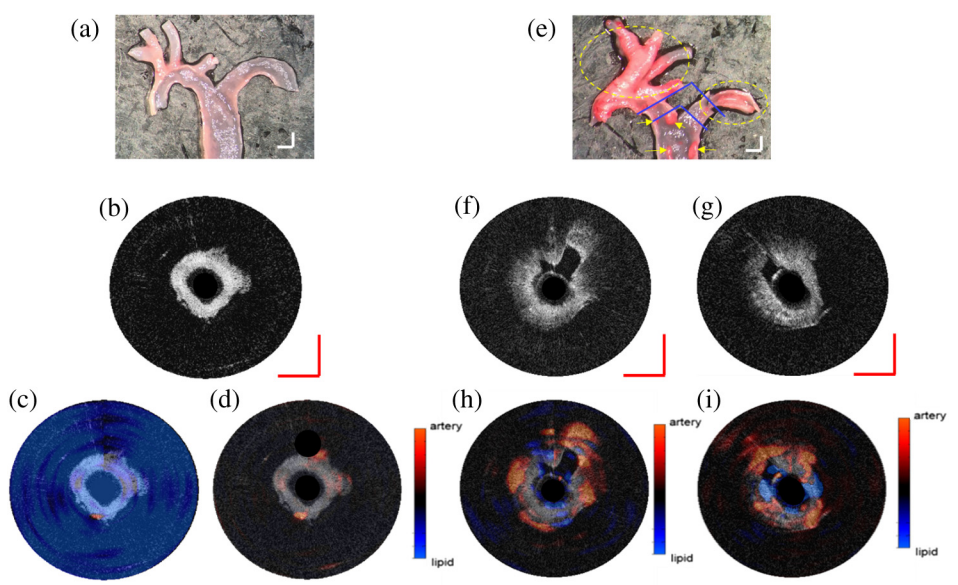

Fig. 9 Imaging results of the mouse model. (a)–(d) healthy aorta microscope photograph, conventional OCT image from 1.3 μm band, preprocessed and postprocessed SOCT images, respectively. (e) CAD aorta microscope photograph. (f) and (g) CAD aorta conventional OCT image from 1.3 μm band at two different sites. (h) and (i) SOCT image corresponding to (f) and (g). (a) and (e) captured after Oil Red O staining. Scale bar: 1 mm; yellow arrow and dashed line, lipid; blue line, imaging plane; center of the imaging probe was blocked.

normalizing background color, artery areas can be slightly visualized. On the other hand, this endoscopic SOCT setup visualized dispersed lipid plaques in the diseased model.

Previous dual-band OCT studies mostly deployed a hue saturation value color map to provide extra contrast.[11] Image subtraction between different wavelength bands has been taken to reflect spectroscopic information and colored in different H-value; while intensity information by frequency compounding is reflected by V-value. In this study, by normalizing image intensities that enhances image contrast and processing its derivative, optical property differences can also be visualized. The larger ratio areas derived from $I_{1.3}/I_{1.5}$ and $I_{1.5}/I_{1.6}$ ratiometric images correspond to different material types. The filtering process then selects these areas for further color staining. The disunity of color region and the material morphology in both Figs. 8 and 9 appears mainly because of the empirical spatial filtering threshold and speckle noise.

This SOCT model is essentially based on contrast comparison between different wavelengths. Some OCT comparisons by two separate bands have been demonstrated by other groups.[21–23] Benjamin et al. launched same incident power on the sample; however, Kodach et al. cast different power from two bands to allow an equal amount of photons from the sample. These investigations indicated that strict power control can showcase the materials' optical property, even without intensity normalization. Recently, Chong et al. also have quantitatively compared signal attenuation characteristics of 1.7 μm OCT for deep tissue brain imaging with other two visible and near-infrared wavelengths. As this unconventional wavelength band showcases a distinctive property of water absorption, lipid contrast, and tissue scattering, it is expected that more wavelength bands will provide better specificity in tissue characterization. In this proof-of-concept work, we have demonstrated the capability of tri-band SOCT in visualizing lipid and artery distribution qualitatively. Referring to the quantitative evaluations of analytes carried out by others through analyzing dual-band signals[24,25] and single-band signal based on a scattering model,[26] further improvements such as strict power control, dynamic focusing, and depth-related compensation[26,27] are expected to be incorporated in this tri-band SOCT system, with which it can help to extract accurate quantitative diagnostic information.

5 Conclusion

In summary, we have developed a tri-band SOCT based on FDML and fiber OPA. This system realizes the qualitative visualization of lipid and artery distribution. The working principle is illustrated by attenuation coefficients differences between different wavelength bands. The swept source in the OCT system has tri-band centers—at 1315, 1509, and 1605 nm—with tens to a hundred nanometer sweeping range at each band. *Ex vivo* lipid and artery functional imaging was subsequently demonstrated with porcine and mouse artery models by image processing from the three bands. This preliminary result could be further improved by time-multiplexing technique, additional wavelength bands, quantitative measurement capability, and real-time processing to advance the progression toward clinical applications.

Acknowledgments

This work was supported by Hong Kong Research Grants Council (Project No. HKU 7172/12E, HKU 17208414, HKU 17205215) and ITF Tier 3 Project (ITS/189/13). Sincere thanks should go to Dr. Jianbing Xu for the fruitful discussions. We also very much appreciate Ms. Jin Li from the Li Ka Shing Faculty of Medicine, The University of Hong Kong for helping us with the animal experiments and discussion.

References

1. W. Drexler and J. G. Fujimoto, *Optical Coherence Tomography: Technology and Applications*, 1st ed., pp. 889–1324, Springer Berlin Heidelberg, New York (2008).
2. G. J. Tearney et al., "Consensus standards for acquisition, measurement, and reporting of intravascular optical coherence tomography studies," *J. Am. Coll. Cardiol.* **59**(18), 1058–1072 (2012).
3. Z. Chen and J. Zhang, "Doppler optical coherence tomography," in *Optical Coherence Tomography: Technology and Applications*, W. Drexler and J. G. Fujimoto, Eds., 1st ed., pp. 621–652, Springer Berlin Heidelberg, New York (2008).
4. D. J. Faber et al., "Light absorption of (oxy-)hemoglobin assessed by spectroscopic optical coherence tomography," *Opt. Lett.* **28**(16), 1436–1438 (2003).
5. J. M. Schmitt, S. H. Xiang, and K. M. Yung, "Differential absorption imaging with optical coherence tomography," *J. Opt. Soc. Am. A* **15**(9), 2288–2296 (1998).
6. U. Morgner et al., "Spectroscopic optical coherence tomography," *Opt. Lett.* **25**(2), 111–113 (2000).
7. J. R. Maher et al., "In vivo analysis of burns in a mouse model using spectroscopic optical coherence tomography," *Opt. Lett.* **39**(19), 5594–5597 (2014).
8. M. Tanaka et al., "1.7-μm spectroscopic spectral-domain optical coherence tomography for imaging lipid distribution within blood vessel," *Opt. Express* **23**(5), 6645–6655 (2015).
9. C. P. Fleming et al., "Depth resolved detection of lipid using spectroscopic optical coherence tomography," *Biomed. Opt. Express* **4**(8), 1269–1284 (2013).
10. A. Federici and A. Dubois, "Three-band, 1.9-μm axial resolution full-field optical coherence microscopy over a 530–1700 nm wavelength range using a single camera," *Opt. Lett.* **39**(6), 1374–1377 (2014).
11. P. Cimalla et al., "Simultaneous dual-band optical coherence tomography in the spectral domain for high resolution in vivo imaging," *Opt. Express* **17**(22), 19486–19500 (2009).
12. M. Tsai and M. Chan, "Simultaneous 0.8, 1.0, and 1.3 μm multispectral and common-path broadband source for optical coherence tomography," *Opt. Lett.* **39**(4), 865–868 (2014).
13. R. Zhu et al., "Dual-band time-multiplexing swept-source optical coherence tomography based on optical parametric amplification," *IEEE J. Sel. Top. Quantum Electron.* **18**(4), 1287–1292 (2012).
14. J. Xu et al., "Simultaneous dual-band optical coherence tomography for endoscopic applications," *J. Biomed. Opt.* **19**(12), 126007 (2014).
15. R. Huber, M. Wojtkowski, and J. G. Fujimoto, "Fourier domain mode locking (FDML): a new laser operating regime and applications for optical coherence tomography," *Opt. Express* **14**(8), 3225–3237 (2006).
16. M. E. Marhic et al., "Broadband fiber optical parametric amplifiers," *Opt. Lett.* **21**(8), 573–575 (1996).
17. C. Xu et al., "Separation of absorption and scattering profiles in spectroscopic optical coherence tomography using a least-squares algorithm," *Opt. Express* **12**(20), 4790–4803 (2004).
18. N. Bosschaart et al., "Quantitative comparison of analysis methods for spectroscopic optical coherence tomography," *Biomed. Opt. Express* **4**(11), 2570–2584 (2013).
19. K. S. Meir and E. Leitersdorf, "Atherosclerosis in the apolipoprotein E-deficient mouse, a decade of progress," *Arterioscler. Thromb. Vasc. Biol.* **24**(6), 1006–1014 (2004).
20. T. Klein et al., "Multi-MHz retinal OCT," *Biomed. Opt. Express* **4**(10), 1890–1908 (2013).
21. B. R. Benjamin et al., "Recent developments in Fourier domain mode locked lasers for optical RT coherence tomography: imaging at 1310 nm vs. 1550 nm wavelength," *J. Biophotonics* **2**(6–7), 357–363 (2009).

22. V. M. Kodach et al., "Quantitative comparison of the OCT imaging depth at 1300 nm and 1600 nm," *Biomed. Opt. Express* **1**(1), 176–185 (2010).
23. S. P. Chong et al., "Noninvasive, in vivo imaging of subcortical mouse brain regions with 1.7 μm OCT," *Opt. Lett.* **40**(21), 4911–4914 (2015).
24. U. S. Sathyam et al., "Evaluation of optical coherence quantitation of analytes in turbid media by use of two wavelengths," *Appl. Opt.* **38**(10), 2097–2104 (1999).
25. M. Pircher et al., "Measurement and imaging of water concentration in human cornea with differential absorption optical coherence tomography," *Opt. Express* **11**(18), 2190–2197 (2003).
26. D. J. Faber et al., "Quantitative measurement of attenuation coefficients of weakly scattering media using optical coherence tomography," *Opt. Express* **12**(19), 4353–4365 (2004).
27. M. Zhang, L. Ma, and P. Yu, "Dual-band Fourier domain optical coherence tomography with depth-related compensations," *Biomed. Opt. Express* **5**(1), 167–182 (2014).

Luoqin Yu received her BS degree in optical science and engineering from Fudan University, Shanghai, China, in 2013. She has just obtained her Master of Philosophy degree in the Department of Electrical and Electronic Engineering (EEE), The University of Hong Kong (HKU), Hong Kong, under the supervision of Dr. Wong. Her research interests include Fourier domain mode-locked laser, optical time-stretch, and swept source optical coherence tomography.

Jiqiang Kang received his BS degree in optical information science and technology from Wuhan University of Technology, China, in 2011, and M Eng degree in precision instrument from Tsinghua University, Beijing, China, in 2014. He is currently working towards his PhD degree in EEE at HKU, under the supervision of Dr. Wong. His research interests include fiber optical parametric amplifier and optical coherence tomography.

Chandra Jinata obtained his BSc degree in microbiology with the highest distinction from Bandung Institute of Technology, Indonesia, in 2011 and has recently finished his M Phil study in bioengineering from The Hong Kong University of Science and Technology (HKUST), Hong Kong. Currently he works as a research assistant at EEE Department, HKU, under the supervision of Dr. Wong. His research interest includes imaging modality utilization toward biomedical application.

Xie Wang: Biography is not available.

Xiaoming Wei received his BS and MS degrees as excellent graduate student from South China University of Technology, Guangzhou, China, in 2009 and 2012, respectively. His master's thesis was awarded excellent master thesis of Guangdong province. He has just completed his PhD degree under Dr. Wong's supervision in EEE Department at HKU. His current postdoctoral research includes femtosecond mode-locked fiber laser, fiber optical parametric amplifier/oscillator, broadband swept laser source, ultrafast microscopy, tomography, and spectroscopy

Kin Tak Chan received his BS, MS, and PhD degrees in biology from HKUST, in 1997, 1999, and 2004, respectively. He is currently a senior technical officer in the Department of Surgery, Li Ka Shing Faculty of Medicine, HKU. His research interests include animal disease models establishment and their imaging system.

Nikki P. Lee obtained her BSc (first class honors) and Ph D degrees from HKU in 2000 and 2003, respectively. She is currently an assistant professor of the Department of Surgery, Li Ka Shing Faculty of Medicine, HKU. Her research interest focuses on translational cancer research, which involves esophageal and liver cancers. The topic is mainly on the research and development of cancer biomarkers and therapeutic targets.

Kenneth K. Y. Wong received his BE (1st class honor with medal award) degree in electrical engineering and BS degree in physics from The University of Queensland, Australia, in 1997. He received his MS in 1998 and PhD degree in 2003, both in electrical engineering at Stanford University. He is currently an associate professor in the EEE Department at HKU. His research includes fiber nonlinearity, fiber optical parametric amplifiers, microwave photonics, and biophotonics.